

Electromagnetic emissions in the MHz and GHz frequency ranges driven by the streamer formation processes

E. V. Parkevich^{1,*}, A. I. Khirianova,¹ T. F. Khirianov,¹ I. S. Baidin,¹ K. V. Shpakov,¹ A. A. Rodionov,¹ Ya. K. Bolotov,^{2,1} V. A. Ryabov,¹ Yu. K. Kurilenkov³, I. S. Samoylov³, S. A. Ambrozevich⁴ and A. V. Oginov¹

¹*P. N. Lebedev Physical Institute of the Russian Academy of Sciences, 53 Leninskiy Prospekt, Moscow 119991, Russia*

²*Moscow Institute of Physics and Technology, Institutskiy Pereulok 9, Dolgoprudny, Moscow Region 141700, Russia*

³*Joint Institute for High Temperatures, Russian Academy of Sciences, Izhorskaya Street 13/2, Moscow 125412, Russia*

⁴*Bauman Moscow State Technical University, 5/1 2-ya Baumanskaya Street, Moscow 105005, Russia*

 (Received 7 April 2022; revised 26 August 2022; accepted 29 September 2022; published 28 October 2022)

We provide comprehensive data on the spectral and temporal characteristics of low-frequency (LF) (MHz) and high-frequency (HF) (GHz) radio emissions and investigate their correlation with the streamer formation. We show that the propagation of streamers from the cathode is accompanied only by the LF radio emission (10–150 MHz). In contrast, the HF radio emission (1–4 GHz) arises during the travel of counterstreamers from the anode, which is also indicated by radio interferometric measurements. The power of the LF radio emission sharply increases almost synchronously with that of the HF radio emission. We find that the HF radio emission has a complex spectral and temporal structure and appears as multiple short (less than 1 ns) bursts characterized by various frequency components, existing in subnanosecond time intervals.

DOI: [10.1103/PhysRevE.106.045210](https://doi.org/10.1103/PhysRevE.106.045210)

I. INTRODUCTION

Radio emission produced by laboratory and atmospheric discharges is a very interesting phenomenon studied by many research groups worldwide. Being driven by intense plasma formation processes, radio emission contains information about the discharge structure and can be used for real-time monitoring of lightning events, as well as estimating the discharge characteristics inside thunderclouds. In the majority of studies in this field, radio emission was analyzed in the MHz frequency range (~ 10 – 100 MHz) [1–6]. The high-frequency (HF) radio emission (at frequencies greater than 1 GHz) was studied mainly at particular frequencies employing narrow bandpass filters (with a bandwidth of about several tens of MHz) [7–11]. Only recently, first observations of intense microwave bursts from long (of about 1 m) spark discharges in an ultrawideband (1–10 GHz) were reported in [12]. The achievement of the maximum power of the bursts (at 2–5 GHz) was associated with streamer flashes during the leader development. To date, the head-on collisions of numerous opposite-polarity streamers are assumed to provoke the intense generation of microwave radiation in the MHz and GHz frequency ranges due to very rapid current variations. According to the simulations in [13,14], the appearance of the low-frequency (LF) emission ($\sim 10^7$ – 10^8 Hz) is inherent to propagating streamers, whereas intense emissions greater than 1 GHz are mainly caused by the collisions of opposite polarity streamers as well as by corona flashes at the head of a stepped leader in a lightning discharge. The simulation results correlate with the modern experimental data [3,8,12,15]. Indeed, a particular correlation between the appearance of

intense microwave bursts and x rays was observed in the experiments. In [7] the authors established that the achievement of the maximum power of microwave emission at 2.4 GHz coincides with the instant the x-ray generation starts in the discharge. However, the streamer capability to produce strong radio emission is still poorly understood due to a lack of experimental data, especially in the GHz frequency range. This fact challenges the elaboration of consistent models used to describe the mechanisms of intense microwave emissions in discharges. Therefore, our study is aimed at revealing the discharge breakdown processes that are able to emit broadband radio emissions, as well as investigating the radio emission properties in detail.

In this paper we thoroughly analyze the spectral and temporal characteristics of the LF and HF radio emissions and investigate their correlation with the discharge evolution. We also perform radio interferometric measurements and thereby localize the discharge zones related to the onsets of the HF radio emissions. Our study reveals a close relationship between the radio emissions and the intense development and multiplication of multiple opposite-polarity streamers in the discharge.

II. EXPERIMENTAL SETUP

We investigate HF and LF radio emissions from a laboratory discharge initiated in a 50-cm gap by applying a 1-MV pulse (negative polarity) with a 1- μ s duration and a rise time of about several hundred nanoseconds. The discharge develops in air at normal conditions in the gap formed by a needle-inside-cone-type cathode and a hemispherical wire mesh anode (Fig. 1). The employed generator was described in detail in [16] together with the devices used for electrophysical measurements.

*Corresponding author: parkevich@phystech.edu

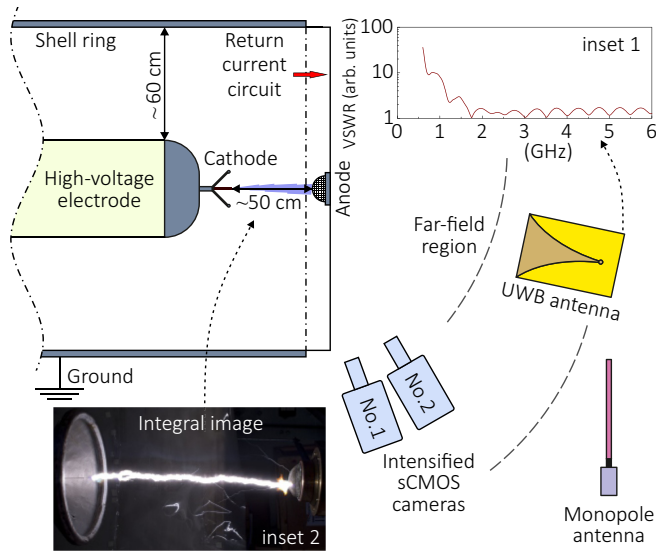


FIG. 1. Experimental setup and devices employed for registering electromagnetic emissions and imaging the discharge. Inset 1 presents the simulated voltage standing-wave ratio of the ultrawideband antenna. Inset 2 shows the integral image of the discharge in the gap, formed by a needle-inside-cone-type cathode and a hemispherical wire-mesh anode.

In the MHz frequency range, we detect LF radio emissions by a single monopole antenna (Tektronix 119-6609-00), with its bandwidth and resonant frequency being 5–1080 and 136 MHz, respectively. The HF radio emissions are registered by an ultrawideband Vivaldi-type antenna [17], which is installed at a distance of 3 m (in the Fraunhofer zone) from the discharge on dielectric tripods and has a vertical polarization. The simulated voltage standing-wave ratio (VSWR) of the antenna is shown in the inset 1 of Fig. 1. The ratio falls within 1–2 at 1–10 GHz and sharply increases at less than 1 GHz; hence microwave emissions are reliably registered at frequencies greater than 1 GHz. The signals from the monopole and Vivaldi-type antennas are recorded by a LeCroy WM8620A oscilloscope (6 GHz, 20 GSa/s). In special experiments, we perform radio interferometric measurements by employing four identical Vivaldi-type antennas, which are placed in the far-field region at different distances from the discharge gap and cover its key sectors.

We also monitor the chronology of the discharge development by employing two scientific complementary metal-oxide-semiconductor (sCMOS) gated intensified cameras (PCO dicam C1). Each camera has a 50–60 ns gate and is coupled with a Canon EF 85-mm $f/1.8$ objective covered with a bandpass optical filter (300–400 nm). The cameras are placed close to each other and image the discharge at an angle of view of approximately 60° – 70° with respect to the gap axis, as shown in the inset 2 of Fig. 1. The cameras are synchronized and record the images of the discharge glow with a tunable delay.

III. INSIGHT INTO THE DISCHARGE DEVELOPMENT

Figure 2 shows three key stages (frames 1–3) of the discharge development falling within the rise time (~ 200 ns) of

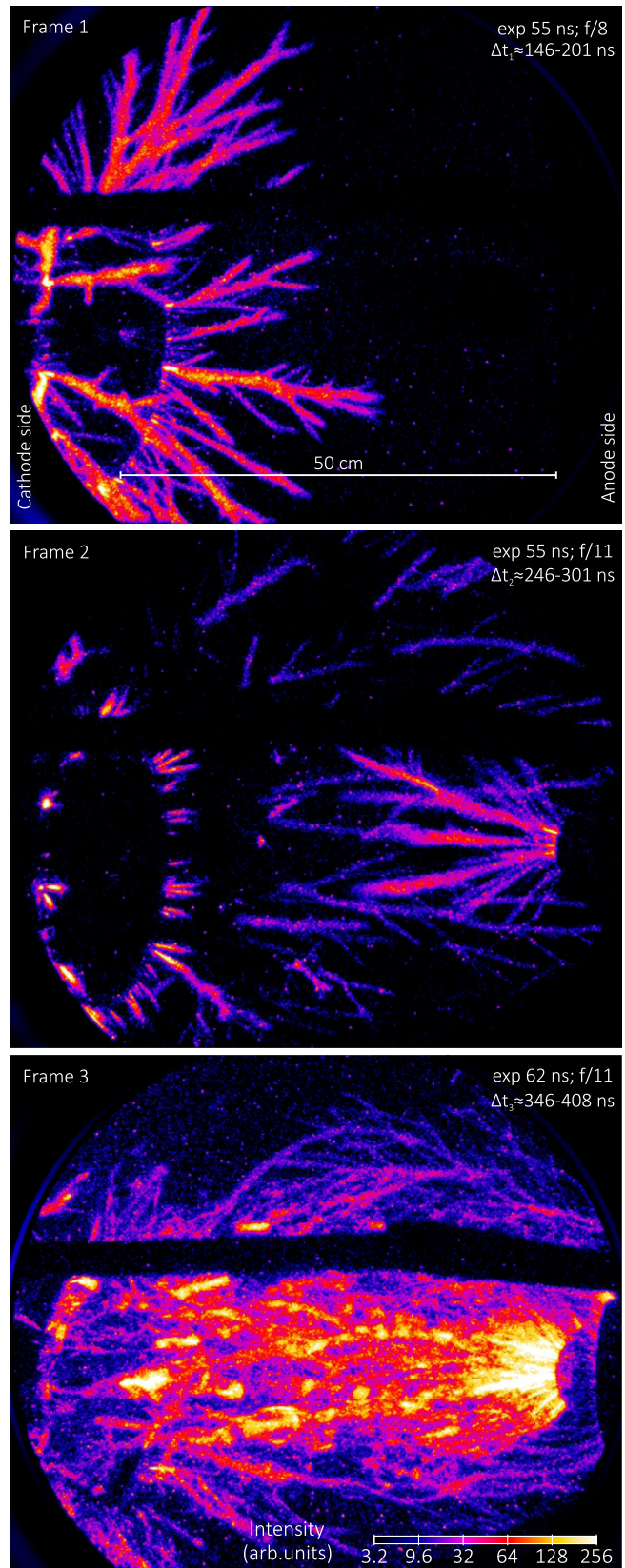


FIG. 2. Images are obtained in different shots and illustrate streamers propagating towards the anode (frame 1), counterstreamers traveling to the cathode (frame 2), and a complex net of numerous plasma channels resulting from the intense development of streamers in the discharge bulk (frame 3). Here exp denotes the exposure time.

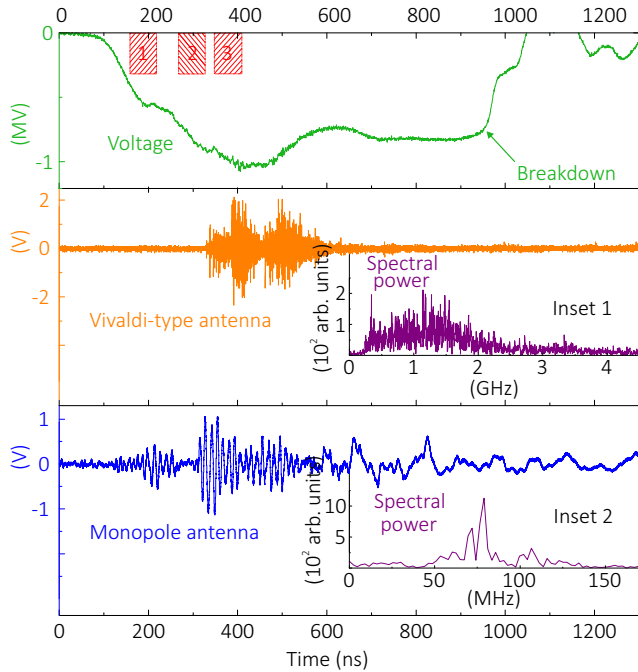


FIG. 3. Voltage waveform, microwave signals, and their spectra (insets 1 and 2) obtained in a single discharge event. Digits 1–3 in the top panel indicate the time intervals Δt_1 , Δt_2 , and Δt_3 associated with the discharge images in Fig. 2.

the applied voltage pulse. The frames are recorded in independent discharge events during different time periods, which are marked in Fig. 3 together with a characteristic voltage waveform, microwave signals, and their spectra (insets 1 and 2) obtained in a single discharge event. Each discharge structure in frames 1–3 is characteristic of a considered time period of the discharge evolution owing to the good repeatability of the discharge development in time and space from shot to shot and the stable temporal characteristics of the employed high-voltage generator.

It is seen that, during the rise of the discharge voltage, an extended cathode corona and multiple streamers develop from the cathode cone edge and needle (see frame 1 in Fig. 2). The streamers propagate towards the anode in a wide solid angle with an average velocity of 10^8 cm/s and branch in some areas. The streamer heads and tails are separated from the bright cathode corona locked to the cone edge (see frame 2 in Fig. 2). When the anode-directed streamers come close to the anode surface, very fast formation of the cathode-directed streamers starts (frame 2 in Fig. 2); these streamers propagate towards the cathode with a characteristic velocity much faster than 10^8 cm/s. The streamer development and multiplication in the discharge bulk give rise to a complex system of plasma channels (see frame 3 in Fig. 2), which spans the entire discharge gap. One can assume the plasma medium in frames 2 and 3 in Fig. 2 to be characterized by the head-on collisions of multiple opposite-polarity streamers and probable origination of secondary streamers in local discharge zones corresponding to the branching points of primary anode- and cathode-directed streamers [18].

The fast development of streamers from the electrodes is accompanied by the generation of short microwave bursts in the MHz and GHz frequency ranges. In the case at hand, the microwave emission is assumed to be associated with rapid current and electric-field changes in the zones of intense plasma formation. Statistics show that the stage of the intense development of the anode-directed streamers (see frame 1 in Fig. 2) is accompanied by the LF radio emission only (see Fig. 3). Here one can assume the discharge regions filled with the growing streamers to be responsible for triggering LF radio emissions. In contrast, the HF radio emission appears with a 200-ns delay (relative to the LF radio emission) and falls within (in the first approximation) the discharge stage when first streamers originate at the anode surface and start to travel towards the cathode. Remarkably, the power of the LF radio emission sharply increases almost synchronously with the appearance of the HF radio emission. After this, the entire discharge gap is assumed to emit the LF radio emission. Both radio emissions decay to 600 ns, with total durations of the emissions being of approximately 430 and 300 ns for the MHz and GHz frequency ranges, respectively.

IV. COUNTERSTREAMERS TRAVELING TOWARDS THE CATHODE

The appearance of intense flashes of the HF radio emission is assumed to be owed to zones wherein the head-on collisions of streamers with the opposite polarity occur. At least this is indicated by the theoretical considerations in [13,14]. Taking into account the rapid development of counterstreamers from the anode, one can expect that precisely such streamers provide a means for the head-on collisions on nanosecond timescales. Therefore, it is important to consider in detail the stage of the discharge development which coincides with the propagation of counterstreamers towards the cathode.

Figure 4 shows the discharge images recorded in different shots by using two sCMOS cameras synchronized with each other with an accuracy of about 0.5 ns. The frames are obtained under similar conditions of the image recording with an exposure time of approximately 51 ns and the relative number of the objectives of $f/8$. The image intensity corresponds to 256 shades of gray represented in the color palette. The delay between two frames, determined as the time period between the instants the signals of the camera shutters fall down up to the noise level, was set to be equal to approximately 5 ns. The short delay between the frames allowed us to trace the fastest changes in the morphology of the discharge structure with a reliable temporal resolution against the integral picture of the discharge registered with the long exposure time. In this way we found that individual branches of a single streamer bush locked to the anode surface propagate with velocities of $(1-2) \times 10^9$ cm/s. Such high velocities of the growing streamers are inherent to those parts of branching streamers that travel in the direction of the cathode needle and cone. In addition, these parts of the cathode-directed streamers turn out to be the brightest with respect to all resolvable discharge structures (with the exception of near-electrode regions) and have the largest diameters, in the range of 1–2 cm. The characteristic velocity of the streamer parts growing in the peripheral region of the discharge gap is several times smaller

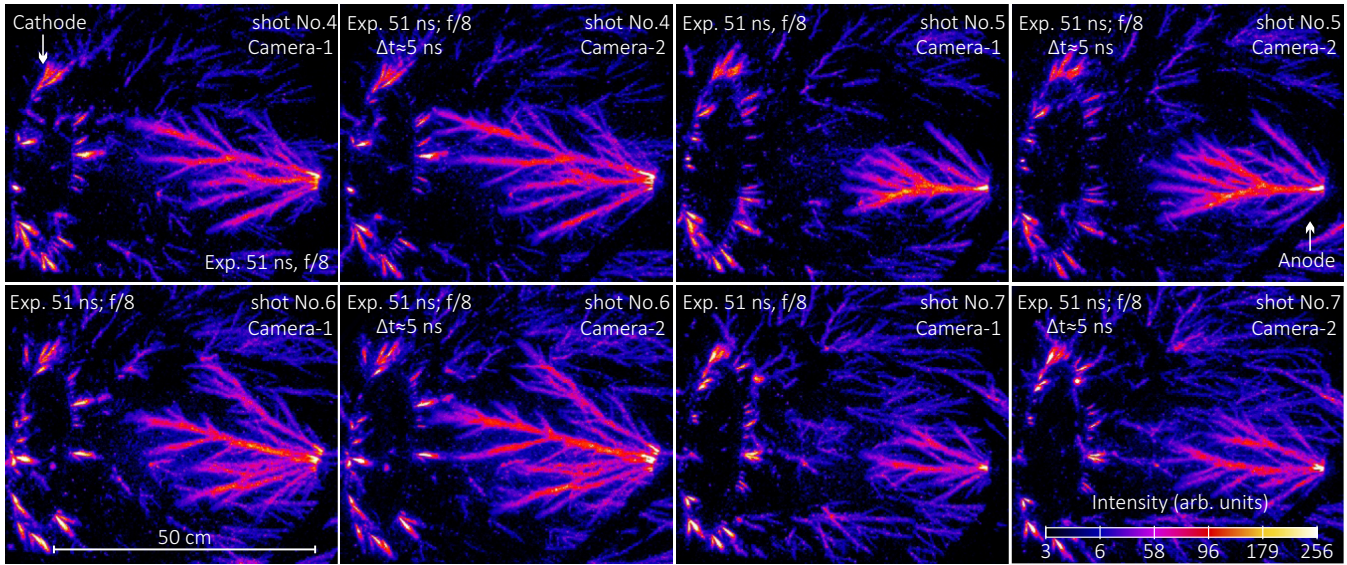


FIG. 4. Discharge images recorded in different shots with the simultaneous use of two sCMOS cameras, both having an exposure time (Exp.) approximately equal to 51 ns and imaging the discharge with $\Delta t \approx 5$ ns delay between the frames.

but still significantly exceeds the average velocity of the streamer propagation from the cathode, of about 10^8 cm/s. The images of the cathode-directed streamers in the peripheral discharge regions are most often dim and their intensity is comparable to that of residual streamers traveling towards the anode. The transverse dimensions of weakly luminous streamer channels are in the range of 0.1–1 cm. During the delay time of 5 ns between two adjacent frames of the developing cathode-directed streamers, the latter manage not only to overcome noticeable distances (up to 10 cm) in space but also to experience a certain number of branching. There is also a tendency of the cathode-directed streamers in creating more branches as these streamers approach the near-cathode region.

V. LOCALIZATION OF HF RADIO EMISSIONS

In order to clarify the relationship between the HF radio emissions and the streamer dynamics, we performed radio interferometric measurements of the discharge zones associated with the onsets of the radio emissions. For this, we employed four ultrawideband Vivaldi-type antennas placed at certain distances from the discharge gap (in the xyz coordinate system, the center of which coincides with the top of the hemispherical anode), as shown in Fig. 5(a). The antennas were installed in the far-field region and covered the key sectors of the discharge space from the anode side. The effective aperture of the antennas provided a means for reliably registering radio emissions from the entire region of the discharge gap. The procedure of the radio signal processing was as follows. For each recorded radio signal, we first determined the instant of the onset of the useful radio signal [see the fragments of radio signals in Fig. 5(a)] and a characteristic noise level before the appearance of the radio emission. Further, from the center of the edge of each antenna, a spherical electromagnetic wave was mentally emitted and started to propagate in the direction of the discharge gap. By determining the areas wherein four spherical waves intersect

each other, we found the coordinates of the discharge points associated with a single (for all antennas) onset of the intense radio emission. On average, the error in determining the coordinates of the corresponding points, taking into account the best match of all four spherical waves, was 3–5 cm (100–150 ps in terms of the electromagnetic wave propagation). Thus, in a single discharge event, we established one small-scale spherical zone associated with the onset of a useful radio signal. Figures 5(b) and 5(c) show the corresponding zones localized in the discharge gap in the eight most successful shots (a number of them are presented in Fig. 4). It is seen that the onsets of the HF radio emissions can fall in the midgap of the discharge or be close to the near-cathode region. There is a spread of the zones in the peripheral region of the discharge, which indicates the stochastic nature of the discharge breakdown processes provoking intense HF radio emissions. One can assume that the localized zones in Figs. 5(b) and 5(c) are related to the areas wherein the first most intense collisions of opposite streamers occurred. As it was noted above (see Fig. 4), when approaching the near-cathode region, the cathode-directed streamers (counterstreamers) experience a great deal of branching and generate many substreamer channels in many directions. In this regard, the probability of collision of the opposite-polarity streamers increases sharply.

VI. RADIO EMISSIONS: TEMPORAL STRUCTURE AND SPECTRUM EVOLUTION

Note that the localization of each individual oscillation of a HF radio signal would provide a means to trace the spatial and temporal evolution of radio emission sources with an accuracy of about several centimeters on subnanosecond timescales. Unfortunately, this is extremely difficult to realize by employing the approach used above to process radio signals. Indeed, the radio signals themselves are broadband and their power is nonuniformly described by the frequencies in the range of 1–6 GHz. This significantly complicates the procedure

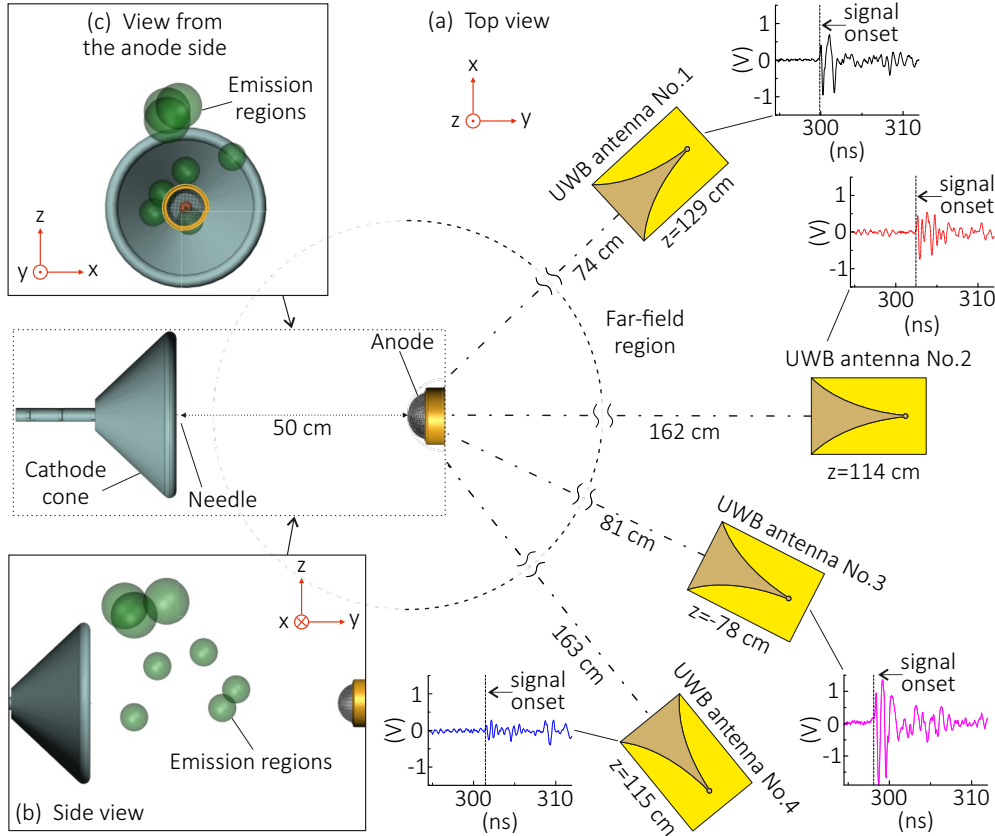


FIG. 5. (a) Scheme of a radio interferometric system, (b) side view of the discharge gap, and (c) view of the gap from the anode side. Superimposed spheres in (b) and (c) are the zones related to the onsets of the intense HF radio emissions localized in eight single shots.

of the radio signal processing even with the employment of the already developed techniques (e.g., see [6]) for analyzing radio flashes. Therefore, it is of particular interest to study in detail the temporal and spectral structure of the recorded HF radio signals and form a basis of their statistical data for further development of advanced techniques of the radio signal processing.

So let us start with Figs. 6 and 7, which demonstrate the spectral and temporal characteristics of the registered microwave signals. Figure 6(a) shows a linearly weighted moving average (WMA) (over 100 ns) $P_{WMA}(t)$ describing the trend in the instantaneous power (squared amplitude) $P(t)$ of the monopole antenna signal in Fig. 3. Figure 6(b) illustrates the spectrum map obtained for the corresponding microwave signal. The map intensity characterizes the values of the average instantaneous power $\bar{P}_f(t)$ in the time and frequency domain (t, f) . For the ultrawideband antenna signal in Fig. 3, a similar moving average (over 1 ns) and spectrum map are shown in Figs. 7(a) and 7(b). The techniques used to obtain the spectral and temporal characteristics of the considered radio signals are described in detail in the Supplemental Material [19].

In Fig. 6(a), within 180–280 ns, one can distinguish a low-power flash of the LF radio emission, which coincides with the stage of the streamer propagation towards the anode. The power of the LF radio emission sharply increases in the time period of 310–410 ns, during which the intense HF radio emission appears. The spectrum of the LF radio emis-

sion in Fig. 6(b) is characterized by the frequencies within 10–150 MHz. The maximum values of $\bar{P}_f(t)$ are reached at 65–85 MHz, which agrees with the integral spectrum in inset 2 of Fig. 3. Compared to the LF radio emission, the HF radio

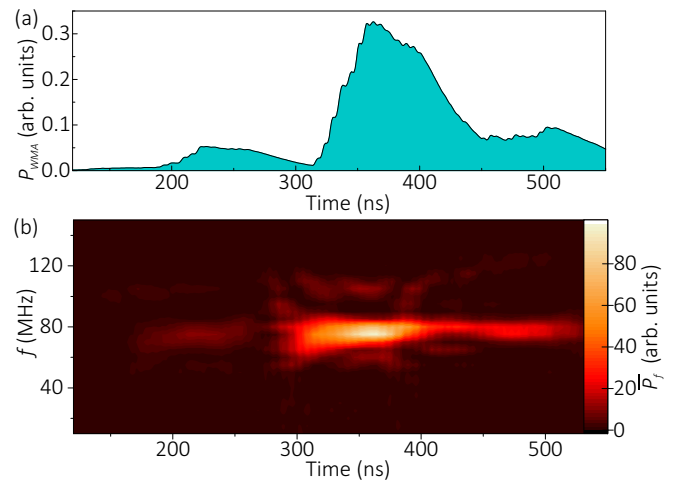


FIG. 6. (a) Weighted moving average (over 100 ns) $P_{WMA}(t)$ of the instantaneous power calculated for the monopole antenna signal in Fig. 3 within 120–550 ns. (b) Map illustrating the evolution of the microwave spectrum in the frequency range of 10–150 MHz. The map intensity characterizes the values of the average instantaneous power $\bar{P}_f(t)$ in the time and frequency domain (t, f) .

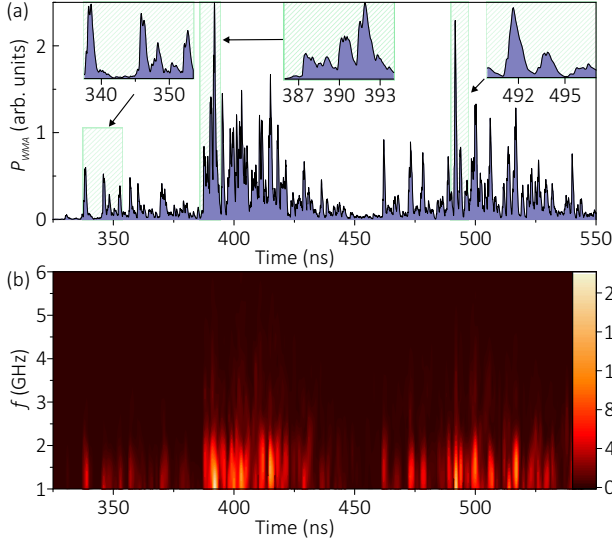


FIG. 7. (a) Weighted moving average (over 1 ns) $P_{\text{WMA}}(t)$ of the instantaneous power calculated for the ultrawideband antenna signal in Fig. 3 within 325–550 ns. (b) Map illustrating the evolution of the microwave spectrum in the frequency range of 1–6 GHz. The map intensity characterizes the values of the average instantaneous power $\bar{P}_f(t)$ in the time and frequency domain (t, f) .

emission has a more complicated spectral and temporal structure. In Fig. 7(a) the entire HF radio signal appears as multiple intense bursts with short durations, which correlate with the bursts in the spectrum map in Fig. 7(b). The majority of the bursts in Fig. 7(b) are characterized by the frequencies of 1–5 GHz, whereas the maximum values of $\bar{P}_f(t)$ are reached at 1–2.5 GHz. Remarkably, a number of the most intense bursts of the HF radio emission fall within 385–395 ns. During this time interval the applied voltage reaches its maximum value, of about 1 MV.

VII. HF RADIO EMISSION: STATISTICAL ANALYSIS

Let us consider Fig. 8(a), which illustrates a certain time period of the instantaneous power $P(t)$ of a typical HF radio signal. The power curve is obtained without averaging and directly shows a number of microwave bursts. A single burst is associated with a particular maximum P^{max} , and the burst duration Δt_{FWHM} is defined as the full width at half maximum. We consider the maximum values only above the noise level (approximately equal to 0.2 arbitrary units) determined statistically within 600–1000 ns. Since many bursts can be merged into a long one, we consider only those cases when, for each P^{max} , there is no secondary maximum in Δt_{FWHM} , i.e., a single burst is fully resolved over Δt_{FWHM} . Such an approach simplifies the statistical analysis and provides reliable data. The delay Δt_{delay} between neighboring bursts is defined as the time interval between the corresponding maxima. This is done to take into account the cases when bursts with distinct maxima follow each other with a short delay but are unresolved in terms of the above criterion. Figure 8(b) shows the average sum $\bar{P}_{\text{WMA}}(t) = 1/20 \sum P_{\text{WMA}}$ of WMA functions (over 1 ns) obtained in 20 discharge events. The function $\bar{P}_{\text{WMA}}(t)$ illustrates the characteristic dynamics of the power

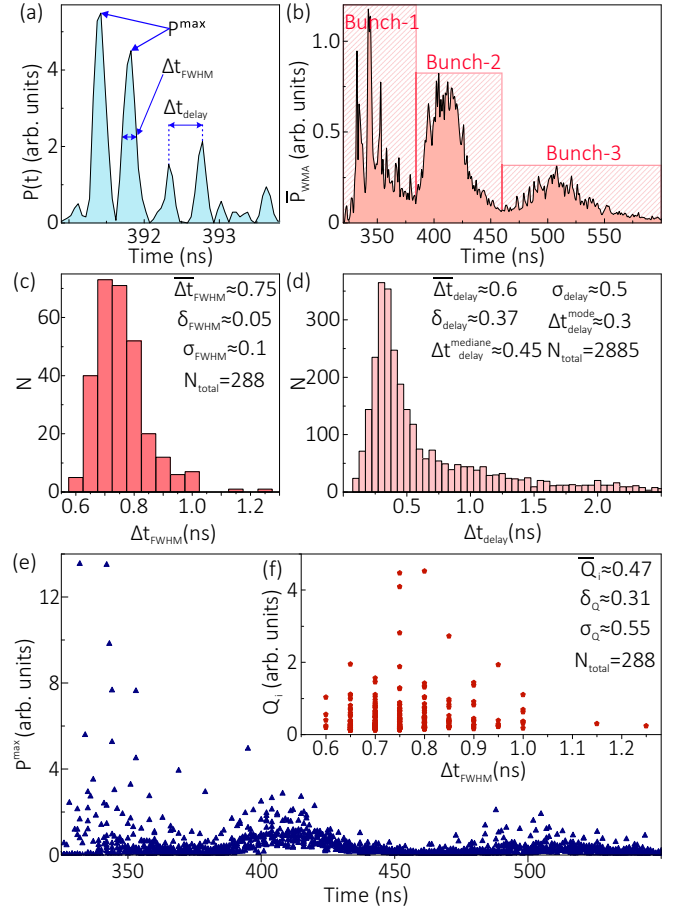


FIG. 8. (a) Certain time period of the instantaneous power $P(t)$ of a typical HF radio signal. (b) Average sum $\bar{P}_{\text{WMA}}(t)$ of WMA functions obtained over 1 ns. (c) Bar chart of the burst duration Δt_{FWHM} . (d) Asymmetric bar chart of the delay Δt_{delay} between the maxima of neighboring bursts. (e) Burst maxima. (f) Scatter plot of the burst energy Q_i depending on the burst duration. Here $\bar{\Delta t}_{\text{FWHM}}$, $\bar{\Delta t}_{\text{delay}}$, and \bar{Q}_i are mean values; δ_{FWHM} , δ_{delay} , and δ_Q are mean deviations; σ_{FWHM} , σ_{delay} , and σ_Q are standard deviations; $\Delta t_{\text{delay}}^{\text{mode}}$ is the mode; $\Delta t_{\text{delay}}^{\text{median}}$ is the median; and N_{total} is the total number of observations. The data are obtained in 20 discharge events.

curve in a single discharge event and reveals three approximately (100–200)-ns-long bunches that set the global trend in the signal power. The bunchlike temporal structure of the HF radio emission may be related to the stepwise character of the discharge formation, e.g., with the steplike generation of streamers from the electrodes or inside the discharge gap, which trigger HF radio emissions. Figure 8(c) shows the bar chart of the burst durations Δt_{FWHM} obtained in 20 discharge events. Herein we have reliably resolved $N_{\text{total}} = 288$ single bursts, with their average duration being $\bar{\Delta t}_{\text{FWHM}} \approx 0.75$ ns (the average and standard deviations are $\delta_{\text{FWHM}} \approx 0.05$ ns and $\sigma_{\text{FWHM}} \approx 0.1$ ns). So, almost all single bursts are shorter than 1 ns. Figure 8(d) presents the bar chart obtained for the delay Δt_{delay} between the maxima of neighboring bursts. The bar chart is asymmetric and can be characterized by the mode, median, and mean, with their values being $\Delta t_{\text{delay}}^{\text{mode}} \approx 0.3$ ns, $\Delta t_{\text{delay}}^{\text{median}} \approx 0.45$ ns, and $\bar{\Delta t}_{\text{delay}} \approx 0.6$ ns (with $\delta_{\text{delay}} \approx$

0.37 ns and $\sigma_{\text{delay}} \approx 0.5$ ns), respectively. The bursts most often follow each other rapidly, but a number of successive bursts can have a delay of the order of a few nanoseconds [see the long tail of the distribution in Fig. 8(d)]. For $2.5 \text{ ns} < \Delta t_{\text{delay}} < 7$ ns, the number of resolved bursts ranges from 0 to 10. Since most bursts have delays within 0.1–2.5 ns, the statistical data in Fig. 8(d) have been calculated only for this delay range. Figure 8(e) demonstrates the scatter plot of the burst maxima. It is seen that the character of the burst localization correlates with three bunches of the HF radio emission in Fig. 8(b). Indeed, the majority of the most intense bursts fall within the first bunch. Probably, the processes which trigger HF radio emissions are strongest during first 100 ns after the emission onset. Figure 8(f) shows the scatter plot of the burst energy Q_i depending on the burst duration Δt_{FWHM} . Here we consider approximate energy values which are defined as $\int_{\Delta t_{\text{FWHM}}} P(t) dt$. The burst ensemble is characterized by a large scatter in Q_i , although almost all bursts having the highest energy are concentrated around approximately 0.75 ns, associated with the maximum number of burst observations.

Let us turn to a microwave map. Here a single burst appears as a two-dimensional area (limited by an envelope line) wherein the radiation power is higher than the noise level. So the burst should be analyzed in two dimensions at once. It is more informative, however, to reduce the analysis of the burst areas to one-dimensional distributions describing the general behavior of the spectral and temporal characteristics of the HF radio emission. For this we employ the following analysis procedure. We take a microwave map [see Fig. 9(a)] and cut it into the set of spectral intervals Δf^* with a width of 0.5 GHz. For each Δf^* , we look for bursts associated with particular maxima $\bar{P}_j^{\text{max}}(\Delta f^*)$ of the radiation power [see Fig. 9(b)], with their values being above the noise level (10^{-4} arbitrary units for maps); the j index denotes the number of the maximum resolved in the frequency range Δf^* . Only those maxima are considered that satisfy the condition that there is no secondary maximum in the time interval Δt_j^* defined as the FWHM for $\bar{P}_j^{\text{max}}(\Delta f^*)$. The search for maxima $\bar{P}_j^{\text{max}}(\Delta f^*)$ is carried out with a time step of 50 ps over the entire time period of the useful signal. Figure 9(c) shows the number of observations N of the time intervals Δt^* during which the HF radio emission is described by the frequencies in the spectral interval Δf^* . It is seen that the HF radio emission is most often characterized by the bursts with durations $\Delta t^* = 0.1$ –1 ns related to the frequencies in $\Delta f^* = 1$ –1.5 GHz. At this Δf^* , the distribution of $N(\Delta t^*)$ is nonuniform and has two distinct maxima at $\Delta t^* \approx 0.35$ ns ($N \sim 800$) and $\Delta t^* \approx 0.6$ ns ($N \sim 400$). In the case of $\Delta f^* = 1.5$ –2 GHz, bursts are 0.25–0.8 ns long and the majority of them have durations of $\Delta t^* \approx 0.5$ ns ($N \sim 360$) and $\Delta t^* \approx 0.65$ ns ($N \sim 300$). The spectral intervals 2–2.5 and 2.5–3 GHz are characterized by a shift in the maximum of the distribution $N(\Delta t^*)$ towards short burst durations, up to 0.3 and 0.25 ns, respectively. For these Δt^* , the number of resolved bursts is $N = 500$ ($\Delta f^* = 2$ –2.5 GHz) and $N = 400$ ($\Delta f^* = 2.5$ –3 GHz). With a further increase in the frequencies describing the bursts, statistics drop and bursts themselves become extremely short. In the spectral intervals of 3–3.5 and 3.5–4 GHz, the maximum number of resolved bursts is $N \sim 100$ and 200, respectively, at $\Delta t^* \approx 0.2$ ns.

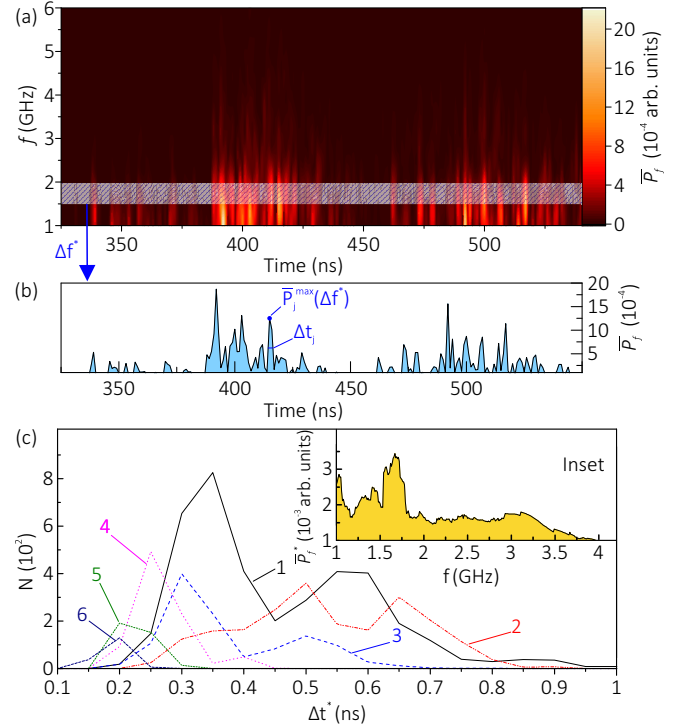


FIG. 9. (a) Illustrative spectrum map of a HF radio signal subjected to tracing in the frequency range of Δf^* , (b) distribution of the average instantaneous power $\bar{P}_j(t)$ extracted for Δf^* , and (c) number of observations N (in 20 discharge events) of the time intervals Δt^* during which the HF radio emission is described by the frequencies in the spectral interval Δf^* (GHz): (1) 1–1.5, (2) 1.5–2, (3) 2–2.5, (4) 2.5–3, (5) 3–3.5, and (6) 3.5–4. The inset shows the average profile \bar{P}_f^* of the burst power depending on frequency f .

Almost all bursts characterized by the frequencies within 3–4 GHz have durations $\Delta t^* = 0.1$ –0.3 ns. Thus, the HF radio emission appears as multiple short (less than 1 ns) bursts with a variety of temporal and spectral characteristics, but the higher the frequency describing the burst is, the shorter the time interval is related to this frequency.

Speaking of microwave bursts in the time and frequency domain, it is of interest to calculate a characteristic profile of the burst power as a function of frequency. We obtained such a profile \bar{P}_f^* in the inset of Fig. 9(c) by analyzing the power maxima $\bar{P}_{\Delta f^*}^{\text{max}}$ in spectral intervals Δf^* with a width of 10 MHz. The width of Δf^* was reduced to achieve smooth changes in the shape of \bar{P}_f^* . For each Δf^* , in 20 discharge events, we looked for the maxima above the noise level (similar to the approach above) and then calculated their average $\bar{P}_f^* = 1/M \sum_{j=1}^M \bar{P}_j^{\text{max}}(\Delta f^*)$. It is seen in the inset that the characteristic burst profile \bar{P}_f^* is nonuniform. The highest value of the burst power is achieved at 1–2 GHz and herein there is a pronounced maximum at approximately 1.67 GHz. In the range of 2–3.2 GHz, the power remains almost constant and then gradually decreases to the noise level at 4 GHz. The effective spectrum of a single microwave burst can be limited from above by $f = 3.5$ GHz.

VIII. DISCUSSION

Our findings indicate that the generation of LF and HF radio flashes is driven by the streamer formation processes. During the early stage of the discharge evolution, the streamer formation can be considered in two characteristic stages. The first stage is associated with the initiation of a large number of streamers at the cathode and their propagation towards the anode. This stage lasts for about 200 ns, with the average propagation velocity of the anode-directed streamers being about 10^8 cm/s, and is accompanied only by the LF radio emission (in the form of an approximately 100-ns prepulse relative to the entire useful signal of the LF radio emission). The spectrum of the LF radio emission is characterized by the frequencies within 10–150 MHz and the maximum power of the radiation is reached at 65–85 MHz. This may be a characteristic of the development of streamer flashes from the electrodes, which are considered to be an analog of the streamer or corona flashes at the head of a growing leader during the lightning discharge formation. For instance, in [3] the authors found that multiple microwave bursts (less than $10\ \mu\text{s}$ in duration) with frequencies in the range of 30–80 MHz are emitted at each temporal-spatial step of a developing negative leader. The capability of the streamer flashes to produce significant LF radio emissions was also predicted by the theoretical considerations in [13,14].

The second stage of the streamer formation is associated with the origination of counterstreamers at the anode surface and their growing towards the cathode. With high propagation velocities, of the order of 10^9 cm/s, counterstreamers from the anode cross the discharge gap for several tens of nanoseconds on average. When propagating, the counterstreamers actively branch and produce a complex dendritic system of plasma channels directed towards the cathode. Intense HF radio emission appears exactly at the stage the counterstreamers travel towards the cathode. The power of the LF radio emission increases significantly as well. Radio interferometric measurements show that the onsets of the HF radio emissions fall within small-scale spherical zones (3–5 cm in diameter) stochastically spread in the periphery region of the discharge, starting from the midgap of the near-cathode area. We suppose that the localized zones of the onsets of the HF radio emissions are associated with the discharge areas wherein the first most intense head-on collisions of the opposite-polarity streamers occurred. Probably, the HF radio emissions can arise in the near-anode region, but no such events were observed. We think that it is an open question, an in-depth investigation of which should be left for future work together with the formation of an exhaustive statistical database. The same applies to the development of advanced techniques for analyzing the HF radio signals recorded by a broadband high-frequency radio interferometric system. A distinct advantage of such a system is that the radio emission sources can be localized in the dis-

charge with an accuracy of the order of several centimeters. A close analog of such a system may be considered the LOFAR system (the world's largest radio telescope) [6], but the latter is capable of localizing the radio emission sources (provided, e.g., by individual steps of leader channels during a lightning discharge) in the MHz frequency range with an accuracy of about units of meters only.

The performed statistical analysis of the characteristics of the broadband HF radio signals revealed their complex spectral and temporal structure. In particular, we found that the HF radio emission appears as multiple bursts, with their durations and the delay between neighboring bursts both being shorter than 1 ns. The temporal structure of the HF radio emission contains three approximately (100–200)-ns-long bunches that set the global trend in the signal power. The most intense bursts are concentrated in the first bunch, which coincides with the time period of the intense development and multiplication of numerous streamers in the discharge bulk, and their durations are close to approximately 0.75 ns on average. The burst spectrum is characterized by the frequencies within 1–4 GHz but, on average, the spectrum is limited at 3.5 GHz. Statistics show that a single burst of the HF radio emission appears as a complex temporal process characterized by various frequency components, existing in subnanosecond time intervals. In other words, the discharge formation processes, which trigger the HF radio emission at fundamentally high frequencies (3–4 GHz), are extremely short (0.1–0.3 ns) by nature.

Thus, our findings provide deep insight into the discharge stages associated with the intense radio emissions in the MHz and GHz frequency ranges and advance the knowledge of the spectral and temporal characteristics of radio emissions. The statistical data obtained on the characteristics of the radio emissions are highly relevant for the elaboration of consistent models describing the mechanisms of x-ray and microwave emissions observed during both laboratory and atmospheric discharges [1–7,7–15,18,20–24]. Notably, the streamer formation processes are a universal way of many discharge systems to develop under an applied electric field [18,25–27]. There are, however, plenty of questions for the existing streamer theories [13,14,18,20,28–30] concerning the streamer capability to produce significant microwave emissions. Here the key problem is that there is still a lack of relevant measurements of the temporal correlations between the corresponding emissions and the streamer development. We think the results obtained in this study are capable of advancing the established insights into the physics behind the streamers and their accompanying electromagnetic emissions.

ACKNOWLEDGMENT

The study was supported by the Russian Science Foundation (Grant No. 19-79-30086).

[1] B. M. Hare, O. Scholten, J. Dwyer, T. N. G. Trinh, S. Buitink, S. Ter Veen, A. Bonardi, A. Corstanje, H. Falcke, J. R. Hörandel

et al., Needle-like structures discovered on positively charged lightning branches, *Nature (London)* **568**, 360 (2019).

- [2] Y. Pu, S. A. Cummer, and N. Liu, VHF radio spectrum of a positive leader and implications for electric fields, *Geophys. Res. Lett.* **48**, e2021GL093145 (2021).
- [3] B. M. Hare, O. Scholten, J. Dwyer, U. Ebert, S. Nijdam, A. Bonardi, S. Buitink, A. Corstanje, H. Falcke, T. Huege, J. R. Hörandel, G. K. Krampah, P. Mitra, K. Mulrey, B. Neijzen, A. Nelles, H. Pandya, J. P. Rachen, L. Rossetto, T. N. G. Trinh, S. ter Veen, and T. Winchen, Radio Emission Reveals Inner Meter-Scale Structure of Negative Lightning Leader Steps, *Phys. Rev. Lett.* **124**, 105101 (2020).
- [4] B. M. Hare, O. Scholten, A. Bonardi, S. Buitink, A. Corstanje, U. Ebert, H. Falcke, J. R. Hörandel, H. Leijnse, P. Mitra *et al.*, Lofar lightning imaging: Mapping lightning with nanosecond precision, *J. Geophys. Res.: Atmos.* **123**, 2861 (2018).
- [5] N. Y. Liu, O. Scholten, B. M. Hare, J. R. Dwyer, C. F. Sterpka, I. Kolmašová, and O. Santolík, LOFAR observations of lightning initial breakdown pulses, *Geophys. Res. Lett.* **49**, e2022GL098073 (2022).
- [6] O. Scholten, B. M. Hare, J. Dwyer, N. Liu, C. Sterpka, I. Kolmašová, O. Santolík, R. Lan, L. Uhlř, S. Buitink *et al.*, Interferometric imaging of intensely radiating negative leaders, *Phys. Rev. D* **105**, 062007 (2022).
- [7] J. Montanyà, F. Fabró, V. March, O. van der Velde, G. Solà, D. Romero, and O. Argemí, X-rays and microwave rf power from high voltage laboratory sparks, *J. Atmos. Sol. Terr. Phys.* **136**, 94 (2015).
- [8] D. Petersen and W. Beasley, Microwave radio emissions of negative cloud-to-ground lightning flashes, *Atmos. Res.* **135-136**, 314 (2014).
- [9] D. A. Petersen and W. H. Beasley, High-speed video observations of a natural negative stepped leader and subsequent dart-stepped leader, *J. Geophys. Res.: Atmos.* **118**, 12,110 (2013).
- [10] V. Fedorov, Y. A. Frolov, and P. Shishkov, Millimetric electromagnetic radiation of a lightning return stroke, *J. Appl. Mech. Tech. Phys.* **42**, 392 (2001).
- [11] W. D. Rust, P. R. Krehbiel, and A. Shlanta, Measurements of radiation from lightning at 2200 MHz, *Geophys. Res. Lett.* **6**, 85 (1979).
- [12] M. Gushchin, S. Korobkov, I. Y. Zudin, A. Nikolenko, P. Mikryukov, V. Syssoev, D. Sukharevsky, A. Orlov, M. Y. Naumova, Y. A. Kuznetsov *et al.*, Nanosecond electromagnetic pulses generated by electric discharges: Observation with clouds of charged water droplets and implications for lightning, *Geophys. Res. Lett.* **48**, e2020GL092108 (2021).
- [13] F. Shi, N. Liu, J. R. Dwyer, and K. M. Ihaddadene, VHF and UHF electromagnetic radiation produced by streamers in lightning, *Geophys. Res. Lett.* **46**, 443 (2019).
- [14] J. Koile, N. Liu, and J. Dwyer, Radio frequency emissions from streamer collisions in subbreakdown fields, *Geophys. Res. Lett.* **48**, e2021GL096214 (2021).
- [15] M. Urbani, J. Montanyà, O. A. Van der Velde, J. López, M. Arcanjo, P. Fontanes, D. Romero, and J. Roncancio, High-energy radiation from natural lightning observed in coincidence with a VHF broadband interferometer, *J. Geophys. Res.: Atmos.* **126**, e2020JD033745 (2021).
- [16] A. V. Agafonov, V. A. Bogachenkov, A. P. Chubenko, A. V. Oginov, A. A. Rodionov, A. S. Rusetskiy, V. A. Ryabov, A. L. Shepetov, and K. V. Shpakov, Observation of hard radiations in a laboratory atmospheric high-voltage discharge, *J. Phys. D* **50**, 165202 (2017).
- [17] M. Pasternak, in *Proceedings of the 14th International Conference on Advanced Trends in Radioelectronics, Telecommunications and Computer Engineering (TCSET), Lviv-Slavske, 2018* (IEEE, Piscataway, 2018), pp. 624–627.
- [18] P. O. Kochkin, A. P. K. van Deursen, and U. Ebert, Experimental study of the spatio-temporal development of metre-scale negative discharge in air, *J. Phys. D* **47**, 145203 (2014).
- [19] See Supplemental Material at <http://link.aps.org/supplemental/10.1103/PhysRevE.106.045210> for more details.
- [20] P. O. Kochkin, A. P. J. van Deursen, and U. Ebert, Experimental study of hard x-rays emitted from metre-scale positive discharges in air, *J. Phys. D* **45**, 425202 (2012).
- [21] T. Shao, V. Tarasenko, C. Zhang, D. Rybka, I. Kostyrya, A. Kozyrev, P. Yan, and V. Y. Kozhevnikov, Runaway electrons and x-rays from a corona discharge in atmospheric pressure air, *New J. Phys.* **13**, 113035 (2011).
- [22] V. Tarasenko, Runaway electrons in diffuse gas discharges, *Plasma Sources Sci. Technol.* **29**, 034001 (2020).
- [23] M. Rahman, P. Hettiarachchi, V. Cooray, J. Dwyer, V. Rakov, and H. K. Rassoul, Observations of x-rays from laboratory sparks in air at atmospheric pressure under negative switching impulse voltages, *Atmosphere* **10**, 169 (2019).
- [24] C. L. da Silva, R. M. Millan, D. G. McGaw, C. T. Yu, A. S. Putter, J. LaBelle, and J. Dwyer, Laboratory measurements of x-ray emissions from centimeter-long streamer corona discharges, *Geophys. Res. Lett.* **44**, 11 (2017).
- [25] E. van Veldhuizen, P. Kemps, and W. Rutgers, Streamer branching in a short gap: The influence of the power supply, *IEEE Trans. Plasma Sci.* **30**, 162 (2002).
- [26] P. Kochkin, C. Köhn, U. Ebert, and L. van Deursen, Analyzing x-ray emissions from meter-scale negative discharges in ambient air, *Plasma Sources Sci. Technol.* **25**, 044002 (2016).
- [27] R. Ono and T. Oda, Formation and structure of primary and secondary streamers in positive pulsed corona discharge—effect of oxygen concentration and applied voltage, *J. Phys. D* **36**, 1952 (2003).
- [28] G. D. Moss, V. P. Pasko, N. Liu, and G. Veronis, Monte Carlo model for analysis of thermal runaway electrons in streamer tips in transient luminous events and streamer zones of lightning leaders, *J. Geophys. Res.: Space* **111**, A2 (2006).
- [29] S. Celestin and V. P. Pasko, Energy and fluxes of thermal runaway electrons produced by exponential growth of streamers during the stepping of lightning leaders and in transient luminous events, *J. Geophys. Res.: Space* **116**, A3 (2011).
- [30] A. Luque, Radio frequency electromagnetic radiation from streamer collisions, *J. Geophys. Res. Atmos.* **122**, 10,497 (2017).